Evolutionary models for very-low-mass stars and brown dwarfs with dusty atmospheres

G. Chabrier[1,2], I. Baraffe[1,2], F. Allard[1]

and

P. Hauschildt[3]

[1] Ecole Normale Supérieure de Lyon, C.R.A.L (UMR 5574 CNRS),

69364 Lyon Cedex 07, France

email: chabrier, ibaraffe, fallard @ens-lyon.fr

[2] Astronomy department, University of California, Berkeley, CA 94720

[3]Dept. of Physics and Astronomy and Center for Simulational Physics,

University of Georgia Athens, GA 30602-2451

email: yeti@hobbes.physast.uga.edu

Submitted to: *Astrophysical Journal*

Version: May 29, 2000

Received ______________________; accepted ______________________

ABSTRACT

We present evolutionary calculations for very-low-mass stars and brown dwarfs based on synthetic spectra and non-grey atmosphere models which include dust formation and opacity, i.e. objects with $T_{\rm eff} \lesssim 2800$ K. The interior of the most massive brown dwarfs is shown to develop a conductive core after ~ 2 Gyr which slows down their cooling. Comparison is made in optical and infrared color-magnitude diagrams with recent late-M and L-dwarf observations. The saturation in optical colors and the very red near-infrared colors of these objects are well explained by the onset of dust formation in the atmosphere. Comparison of the faintest presently observed L-dwarfs with these dusty evolutionary models suggests that dynamical processes such as turbulent diffusion and gravitational settling are taking place near the photosphere. As the effective temperature decreases below $T_{\rm eff} \approx 1300 - 1400$ K, the colors of these objects move to very blue near-infrared colors, a consequence of the ongoing methane absorption in the infrared. We suggest the possibility of a brown dwarf dearth in J, H, K color-magnitude diagrams around this temperature.

Subject headings: stars: low-mass, brown dwarfs — stars: evolution — stars: colour - magnitude diagrams

1. Introduction

Since the unambiguous identification of the first cool brown dwarf (BD) Gl 229B (Oppenheimer et al. 1995), the discovery of objects with temperatures cooler than the latest known M-dwarfs has been steadily increasing. These discoveries revealed two classes of objects requiring new spectral classifications. On one hand, a family of objects shows very red infrared (J-K, H-K) colors while the signature of metal oxides (TiO, VO), whose band strength index is used to classify M-dwarf spectral types, and hydrides (FeH, CaH bands) disappear gradually from the spectral distribution, as observed e.g. in GD 165B (Kirkpatrick et al. 1999a). Several of these so-called "L" dwarfs (Martín et al. 1999; Kirkpatrick et al. 1999b), have been discovered by the near-IR surveys DENIS (Delfosse et al. 1999) and 2MASS (Kirkpatrick et al. 1999b). On the other hand, a dozen of objects with properties similar to Gl229B have been recently discovered with 2MASS (Burgasser et al. 1999), SDSS (Strauss et al. 1999) and the VLT (Cuby et al. 1999). The IR spectrum of these objects is characterized by the unambiguous signature of methane absorption in the H, K and L bands, the predicted dominant equilibrium form of carbon below a local temperature $T \approx 1300 - 1500$ K in the $P \approx 5 - 10$ bar range (Allard & Hauschildt 1995; Tsuji et al. 1996; Fegley & Lodders 1996). This yields blue near-infrared colors, with $J - K \lesssim 0$ but $I - J \gtrsim 5$ (see e.g. Allard 1999). These cool dwarfs are identified as "methane" dwarfs, sometimes called also "T-dwarfs" (Kirkpatrick et al. 1999b).

The spectroscopic and photometric properties of L-dwarfs and, to less extent, of methane-dwarfs cannot be properly reproduced by dust-free atmosphere models, indicating that below $T_{\rm eff} \lesssim 2800K$, theoretical models must include the formation and the opacity of dust grains (Tsuji et al. 1996, 1999; Ruiz et al. 1997; Jones and Tsuji 1997; Allard 1998; Leggett et al. 1998; Tinney et al. 1998; Basri et al. 1999; Kirkpatrick et al. 1999b).

In previous papers, we have developed a consistent theory of the structure and the evolution of low-mass, dense objects (Chabrier and Baraffe 1997, CB97) based on non-grey dust-free atmosphere models (Hauschildt et al. 1999, HAB99). Evolutionary models derived from this general theory describe successfully various observed properties of M-dwarfs down to the bottom of the main sequence: mass-magnitude relationships, color-magnitude diagrams, mass-spectral type relationships (Chabrier et al. 1996; Baraffe & Chabrier, 1996; Baraffe et al. 1997, 1998, BCAH98). The aim of the present paper is to extend these calculations into the brown dwarf domain by including the effect of grain formation both in the atmospheric equation of state (EOS) and in the opacity for objects with $T_{\rm eff} \lesssim 2800K$. The first comprehensive description of the effect of grain formation on the evolution of BDs was done by Lunine et al. (1989) and has been updated and incorporated in Burrows et al. (1993, 1997) calculations. However only a few grains were included in these calculations and the grain opacity is treated either as a frequency-independent Rosseland mean, implying grey atmosphere conditions, above 1300 K (see Figure 1 of Burrows et al. 1997), or is simply ignored (assuming grains settle immediately below the photosphere) below 1300 K, where non-grey atmosphere models are used. The present calculations extend significantly the number of grain species and include consistently their frequency-dependent opacity in the transfer equation, yielding consistent non-grey atmosphere structure, spectral colors and evolutionary calculations. The models are described in §2, whereas comparison between theory and observation in various color-magnitude diagrams (CMD) is presented in §3. The remaining uncertainties and shortcomings in the theory are discussed in the conclusion.

2. Model description

The main input physics involved in the present calculations has been presented in details in CB97 and BCAH98. The outer boundary conditions between the interior and the non-grey atmosphere profiles are described in CB97. Non-grey atmospheres are a necessary condition when absorption coefficients strongly depend upon frequency, which is the case for all objects below $T_{\rm eff} \sim 5000$ K, the onset of molecular formation. The formation of grains in the present model atmospheres is described briefly in Leggett et al. (1998) and Allard (1999) and in details in Allard et al. (2000a). The equilibrium abundances of each grain species are determined from the Gibbs energies of formation, following the method developed by Grossman (1972). At each temperature and for each condensed phase under consideration, the variable $K_c(T)$ is calculated from the partial pressures of the species i forming the condensate (e.g. Al and O for corundum Al_2O_3), determined by the vapor phase equilibria, $P_i = N_i \mathcal{R}\mathcal{T}$, where N_i is the number of moles of species i and $\mathcal{R}$ is the gas constant. This variable K_c is compared to the equilibrium constant K_{eq}, calculated from the Gibbs energy of formation of the condensate. The abundance of a condensed species is obtained by the condition that this species be in equilibrium with the surrounding gas phase, $K_c \geq K_{eq}$ (Grossman, 1972). The opacities of the grains are calculated from Mie theory (see also Alexander & Ferguson, 1994).

The formation of condensed species depletes the gas phase of a number of molecular species (e.g. VO, TiO, FeH, CaH, MgH) and of refractory elements such as Al, Ca, Ti, Fe, V (Fegley & Lodders, 1996; Allard 1998; Lodders 1999; Burrows & Sharp, 1999), modifying significantly the atmospheric structure and the emergent spectrum. For late M-dwarfs and for massive and/or young BDs, the main cloud formation is predicted to occur near the photosphere (see e.g. Allard 1998; Lodders 1999). The present calculations assume a grain-size distribution in the submicron range (Allard et al 2000a). This general grain treatment is consistent with the observations of the objects near the bottom of and below the MS, namely the DENIS and 2MASS objects (Delfosse et al. 1999; Kirkpatrick et al. 1999b), GD 165B (Kirkpatrick et al. 1999a) and Kelu-1 (Ruiz et al. 1997), which all exhibit strong thermal heating and very red colors. Asides from this complex thermochemistry, grain formation is in fact a dynamical process and involves a balance between various timescales, such as the condensation, evaporation, coagulation, coalescence and convection timescales (see e.g. Rossow 1978), not mentioning the fact that non-equilibrium species might be present, as for example in the atmosphere of Jupiter (Fegley & Lodders 1994). Since such dynamical processes are not incorporated in the theory at the present stage, we elected to conduct calculations under various extreme assumptions.

The first set of models are based on the dust-free "NextGen" model atmospheres (Allard et al. 1996; HAB99) and are the same as in BCAH98. In the second set of models, *all* condensed equilibrium species are included both in the EOS and in the opacity, taking into account dust scattering and absorption in the radiative transfer equation. These models are referred to as "DUSTY" models. The third set of models includes the formation of grains in the atmosphere EOS, thus taking into account the photospheric depletion of dust-forming elements in the gas phase, but not in the transfer equation, therefore ignoring the opacity of these condensates. This case, referred to as "COND" models, mimics a rapid gravitational settling of all grains below the photosphere. This is similar to the Burrows et al. (1997) calculations below $T_{\rm eff} \leq 1300$ K (see above).

As mentioned above, the DUSTY and COND models represent extreme situations which bracket the more likely intermediate case resulting from complex, and presently not understood, thermochemical and dynamical processes.

2.1. Atmosphere profiles

Figure 1 displays P-T atmosphere profiles for $T_{\rm eff}$ = 1800 K, log g=5 and solar composition, under the afore-mentioned different assumptions for the dust treatment. The atmospheric heating due to the large grain opacity (the so-called greenhouse or backwarming effect) in the DUSTY model is clearly visible, and yields a significantly hotter structure.

The effect is dominant in the outer layers, where the spectrum forms, and decreases in the inner layers, where the connection with the interior profile occurs (see also Tsuji et al. 1996). When dust opacity is not taken into account as in the COND models, the inner atmospheric structure is barely affected by the formation of dust and is similar to the dust-free case (NextGen) for this temperature. Only for significantly cooler $T_{\rm eff}$ does dust formation start to affect substantially the inner structure compared to dust-free models.

As indicated in Figure 1, convection occurs only in optically-thick regions ($\tau > 1$), in contrast to hotter objects (see BCAH98). However, this optical depth corresponds to only about one pressure scale height $H_{\rm P}$, or even less, from the photosphere ($\tau \sim 1$) near which occurs the condensation temperature of most grains for objects near the bottom of the MS. Even for the cooler models ($T_{\rm eff} \sim 1000$ K) where convection retreats to deeper layers, the top of the convective zone lies only at a few $H_{\rm P}$ from the photosphere. This can have important consequences on the formation and settling of atmospheric grains. Indeed, turbulent diffusion, as produced for example by overshooting from the convection zone or by advection due to rotation, is a much more efficient mechanism than microscopic diffusion and sedimentation, at least for submicron-size particles. Although the temperature at the top of the convective zone is found to be generally above the condensation temperature of all grains, this turbulent diffusion will efficiently bring material upward to the region of condensation and maintain small-grain layers, which otherwise would have settled gravitationally, in this region. Note that for submicron-size species, the condensation time τ_{cond} is much smaller than other dynamical timescales (see e.g. Rossow, 1978; Lunine et al. 1989). As temperature decreases, the photospheric density increases, more species condense so that the particle density ρ_p increases. Coalescence will become effective in growing large particles ($\tau_{coal}/\tau_{cond} \propto T/\rho_p^2$, Rossow 1978) and the afore-mentioned turbulent mixing could no longer prevent these large particles to fall out rapidly. Moreover the condensation line of some species (e.g. silicates) will drop below the photosphere (see e.g. Lodders 1999).

Within this general scheme, the DUSTY models correspond to a situation with very efficient turbulent mixing, whereas the COND models correspond to a situation where mixing is inefficient compared with sedimentation. Whether this general mechanism, and the related decrease of opacity, can explain the color saturation - and thus smaller backwarming - of the coolest L-dwarfs remains to be quantified correctly. Work in this direction is under progress.

As anticipated from Figure 1, spectral and photometric properties are generally more affected by dust formation than the inner atmospheric structure and thus the evolution, as shown in the next section. This reflects the weak dependence of L and $T_{\rm eff}$ upon opacity for BDs, with $L \propto \kappa^{0.3}$ and $T_{\rm eff} \propto\sim \kappa^{0.1}$ (Burrows & Liebert, 1993).

*** FIGURE 1 ***

2.2. Evolutionary calculations

Evolutionary calculations have been performed for $900 \leq T_{\rm eff} \leq 2800$ K, which corresponds to masses between 0.1 $M_\odot$ and 0.01 $M_\odot$ for ages $10^8 \lesssim t \lesssim 10^{10}$ yr, following the method described in CB97. Figure 2 shows the evolution of $T_{\rm eff}$ as a function of time for various masses and dust treatments. This illustrates the uncertainty expected from dust treatment on the cooling of BDs. For a given age, the differences between the two extreme DUSTY and COND models reach up to ∼10% in $T_{\rm eff}$ and ∼25% in luminosity L. The hydrogen-burning minimum mass (HBMM) is only moderately affected by dust formation. The opacity due to the formation of different grains (e.g. silicates, Al_2O_3, $CaTiO_3$) produces a blanketing effect which lowers the effective temperature and luminosity for a given mass at the bottom of the main sequence, as noted initially by Lunine et al (1989). Models omitting grain opacity (NextGen and COND) yield $m_{\rm HBMM} \sim 0.072\ M_\odot$, $T_{\rm eff}$=1700K,

$\log L/L_\odot = 5 \times 10^{-5}$, whereas DUSTY models yield a slightly lower limit, $m_{\rm HBMM} \sim 0.07$ $M_\odot$, $T_{\rm eff}$=1550 K, $\log L/L_\odot = 4 \times 10^{-5}$, for solar composition. A lower luminosity requires a smaller H-burning nuclear energy in the core to reach thermal equilibrium, thus a lower central temperature and therefore a lower mass, which yields a lower HBMM.

*** FIGURE 2 ***

The present calculations incorporate new conductive opacities by Potekhin et al. (1999) in the interior. These opacities, initially developed for neutron star envelopes and white dwarf cores, improve previous calculations (Hubbard and Lampe, 1969; Itoh et al. 1983 and Mitake et al., 1984; Brassard and Fontaine, 1994) and cover the range of temperatures and densities characteristic of BD interiors. An interesting new property revealed by the present calculations is the growth of a conductive core for the most massive BDs. As these objects cool and contract, their interior becomes more and more degenerate ($\psi = kT/kT_F \approx 3.3 \times 10^{-6}\, T\, (\mu_e/\rho)^{2/3}$, where T_F is the electron Fermi temperature and μ_e is the electron mean molecular weight). Electron conductivity becomes more and more important and becomes eventually the main energy transport mechanism in the central regions, instead of convection. This occurs in the core of old ($t \geq 2$ Gyr) BDs in the mass range 0.03-0.07 $M_\odot$, with a maximum extension of the conductive core $R_{cond}/R_\star \approx 0.6 - 0.7$ for the more massive ones, since the maximum central density occurs near the HBMM (Burrows et al. 1997; Chabrier and Baraffe 2000). In this mass range, the conductive core appears at $t \approx$ 2-3 Gyr, for $\psi \lesssim 0.1$, and increases rapidly, reaching up to 50%-70% of the total mass at 10 Gyr for masses $m \approx 0.05 - 0.06$ $M_\odot$. Figure 3 shows the evolution of the conductive core $M_{cond}/M_\star$ as a function of time for a 0.06 $M_\odot$ BD. We verified that these results still hold, although quantitatively different, when using previously published conductive opacities. These properties are essentially unaffected by the dust treatment in the atmosphere, since evolution depends weakly on it.

*** FIGURE 3 ***

The onset and growth of a conductive core does affect the evolution. Once conduction sets in at the center, it increases dramatically the efficiency of energy transport compared to convection ($v_F >> v_{conv}$, where $v_F = (2kT_F/m_e)^{1/2}$ is the electron Fermi velocity), decreasing the internal temperature gradient and yielding a cooler central temperature for a given energy flux $\mathcal{F}$ ($\nabla T^4 \equiv T_c^4/R \propto \mathcal{F}.\kappa_{cond}$, where κ_{cond} is the conductive opacity). This increases electron degeneracy at the center ($\psi \propto kT$ decreases). In first approximation, retaining only the zero-temperature electron contribution and the kinetic ionic contribution, the radius of a BD can be written $R \simeq R_0(1+\psi)$ where $R_0 = 2.8 \times 10^9 (\frac{m}{M_\odot})^{-1/3} \mu_e^{-5/3}$ cm is the zero-temperature (fully degenerate, $\psi = 0$) radius (Stevenson, 1991). Therefore the more degenerate conductive object contracts towards a slightly smaller radius, yielding a larger release of gravitational energy $\delta\Omega = \int_M P\delta(1/\rho)dm$ within a Kelvin-Helmoltz time.

This larger energy source increases the total binding energy of the star:

$$\delta B(t) = -[\delta\Omega(t) + \delta U(t)] = \int_M Gm\delta(\frac{1}{r})dm - \int_M \delta\tilde{u}dm \qquad (1)$$

where $\tilde{u}$ is the specific internal energy, yielding a larger luminosity L for a given age, i.e. slowing down the cooling time τ of the BD, since:

$$L(t) = \frac{dB(t)}{dt} \quad \Rightarrow \tau(L) = \int_{t_0}^{t} \frac{dB(t')}{L} \qquad (2)$$

where we have neglected the nuclear source of energy arising from some residual hydrogen-burning (see e.g. Figure 2 of Chabrier and Baraffe 2000).

As an example, for a 10 Gyr old 0.06 $M_\odot$ BD, $T_{\rm eff}$ is 15% larger and L is 30% brighter when conduction is taken into account. An effect difficult to verify observationally, however, given the faintness of such old BDs. Note that the onset of a conductive core occurs only for $t \gtrsim 1$ Gyr and is thus inconsequential for the application of the lithium-test, which concerns only younger objects (see e.g. CB97).

3. Color - Magnitude diagrams

In this section, we compare the present models with available observations of late-M, L- and methane-dwarfs in various CMDs. The comparison is limited to objects with known distances. Although trigonometric parallaxes have been determined for several 2MASS and DENIS L-dwarfs (Dahn et al. 2000), the only methane dwarf with known distance is Gl229B.

3.1. Optical CMD

*** FIGURE 4 ***

Figure 4 compares models and various observations in a $M_{\rm V}$-(V-I) CMD. Three L-dwarfs of the Dahn et al. (2000) sample are known to be very close binary systems (Martín, Brandner & Basri 1999; Koerner et al. 1999) with nearly equal mass components and their magnitude is corrected in the CMDs to take into account this property. Models with different dust treatments are displayed for ages of 0.1 Gyr (only for the DUSTY models; short-dash line) and 1 Gyr (solid line). For t > 1 Gyr, DUSTY isochrones are hardly distinguishable from one another in any of the following optical (VRI) and near-IR (JHK) CMDs, although the same masses correspond obviously to different magnitudes, and are not shown for sake of clarity. The properties of the DUSTY models for different ages are displayed in Tables 1-5. Note that we do not give the H-magnitude. Indeed, the present models overestimate the flux in this band and work remains to be done to understand this shortcoming. We also give the lithium-abundance depletion for these models for applications of the lithium-test. The COND models displayed in Figure 4 (long-dash line) cover the mass range between 0.08 $M_\odot$ ($T_{\rm eff}=2350K$) and 0.03 $M_\odot$ ($T_{\rm eff}=1050K$) at 1 Gyr.

For $M_{\rm V}$ brighter than 20 ($T_{\rm eff} \gtrsim 2200$ K), the NextGen models (dash-dot) are significantly bluer by 0.3-0.4 mag in $(V-I)$ than the DUSTY models. This is due to the recent improved TiO line list (Schwenke, 1998) included in the DUSTY atmospheres (Allard et al. 2000a,b), while the NextGen models used the previous line list by Jorgensen (1994). As emphasized in BCAH98, the NextGen models predict too blue (up to ~ 0.5 mag) optical colors compared to observations for $10 \lesssim M_{\rm V} \lesssim 19$ (see Figure 6 of BCAH98). As shown in Figure 4, the new TiO linelist improves significantly this situation (see also Allard et al. 2000b) and confirms the fact that the previous discrepancy stemmed primarily from a lacking source of opacity shortward of 1 μm (cf. §4.2 of BCAH98), and not from a major caveat in the treatment of convection. However, as shown in Figure 4 and Figure 5 below, the situation is not completely satisfactory yet, with a remaining $\sim$ 0.2-0.3 offset in colors at the bottom of the MS.

*** FIGURE 5 ***

The dust effect is clearly seen for $M_{\rm V} \gtrsim 19$, $(V-I) \gtrsim 4.8$, with a much more modest reddening as $M_{\rm V}$ increases ($T_{\rm eff}$ decreases) for the DUSTY and COND models than for the dust-free models. This reflects metal and in particular TiO and VO depletion due to grain formation in the COND and DUSTY atmospheres. These species are two main sources of absorption in the optical in the temperature-range of interest. Note that, although the $(V-I)$ colors are similar, the DUSTY models are significantly fainter than the COND ones for a given mass, revealing the grain *opacity* which is not included in COND models, and the depressed continuum in the optical due to the opacity-induced backwarming and

H_2O dissociation (Allard et al. 2000a). Interestingly enough, the same trend of change of slope in $(V-I)$ colors at $M_V \sim 19$ appears in the available observations, but at a ~ 0.5 mag bluer limit, i.e. $(V-I) \lesssim 4.5$, than the theoretical predictions. This builds confidence in our basic treatment of grain formation but suggests that the gas depletion of the main absorbing species in the optical (TiO, VO, FeH) is underestimated in the present theory. Note in passing the limited interest of the V-band for BD search, with most massive BDs older than 1 Gyr being at $M_V \gtrsim 24$.

The saturation in optical colors is even more drastic in $(R-I)$ (Figure 5), where the DUSTY models yield almost constant $(R-I)$ below $T_{\rm eff} \sim 2300$ K ($M_I \gtrsim 14$) at $(R-I) \sim$2.4-2.5. As seen in the figure, the distribution of various objects observed in these colors at the bottom of and below the main sequence, either in the field or in the Pleiades cluster, not only shows the same saturation effect as predicted by the models but is quantitatively in very good agreement with the predicted colors. As mentioned above, however, the $\sim 0.2-0.3$ mag offset above ~ 2300 K is still present. The COND models predict bluer colors as $T_{\rm eff}$ decreases, and in general more flux in the V, R, I bands at a given $T_{\rm eff}$ than the DUSTY models. This stems from (i) the absence of grain opacity in COND models and (ii) the backwarming effect in the DUSTY models (see Figure 1) which destroys IR-absorbing species such as e.g. H_2, H_2O, allowing more flux to escape at longer wavelengths.

Although the L3.5 dwarf 2MASS-WJ0036159+182 (M_V=21.15, M_R=18.15, M_I=15.92, R-I=2.23)(Reid et al. 1999) seems to be lying on the COND track, it is probably misleading and reveals probable errors in the photometry. Indeed, the near-IR colors of this object are not reproduced by the COND models, but rather by the DUSTY ones (see Figure 6).

3.2. Infra-red CMD

Figure 6 displays the same comparisons in near-IR colors ($J-K$). As already mentioned by Leggett et al. (1998), the DUSTY models give the best fit to IR photometry of L- and very late M-dwarfs. They explain the very red colors characteristic of these objects in terms of the backwarming of the atmosphere due to grain absorption, yielding a reduction of the band strengths of the main IR absorbers, like e.g. H_2O, as proposed initially by Tsuji et al. (1996). Such red colors are impossible to reproduce with dust-free opacity models (NextGen and COND). Note that for M_K brighter than ~ 11, the DUSTY models are slightly bluer in $(J-K)$, by ∼0.1-0.2 mag, than the NextGen models. This arises from the use of different H_2O line lists: Miller et al. (1994) in NextGen and the recent AMES list (Partridge and Schwenke, 1997) in DUSTY models. Although less complete for the higher energy transitions than the AMES line list, the Miller et al. (1994) list yields better agreement between models and IR photometric observations for $T_{\rm eff} \gtrsim 2200$-2300 K (where dust does not affect the colors), since it relies on better potential surfaces for high temperatures (see Allard et al. 2000b for details). Below $T_{\rm eff} \sim 2000$ K, these transitions are no longer important and the more complete AMES water linelist is to be used. Below this temperature, however, dust opacity is the main ingredient which shapes the IR colors, and the choice of the water line list is less crucial for photometric analysis. This illustrates again the remaining shortcomings in the present theory arising from still partially inaccurate molecular opacities, and stresses the need for future improvements in these inputs.

*** FIGURE 6 ***

When dust opacity is neglected (COND and NextGen), near-IR colors become bluer due to strong H_2, H_2O, CO and eventually CH_4 absorption in the H and K-bands. This yields very blue near-IR colors, with $J-K \sim J-H \lesssim 0.5$, as illustrated by the good agreement of Gl229B IR colors with the COND track (see also Burrows et al. 1997). The effect is more pronounced for the COND models because of the lack of TiO absorption, which extends into the J-band at these very low effective temperatures. However, the COND models overestimate the flux at and shortward of $\sim 1\,\mu m$ (V, R, I bands) for Gl229B (Golimowski et al. 1998). The spectrum of GL229B indeed does not show strong indication for dust in its IR spectrum from 1 to 5 μm (Allard et al. 1996; Marley et al. 1996; Tsuji et al. 1996; Oppenheimer et al. 1998), but reveals discrepancies in the optical with dust-free models, as mentioned above. Several solutions have been proposed for this missing source of opacity in the optical, such as a specific haze opacity due to the presence of the nearby star (Griffith et al. 1998) or warm dust layers (Tsuji et al. 1999). These suggestions, however, are based on ad-hoc hypothesis required to fit Gl229B spectrum and lack robust physical grounds. The methane-dwarf SDSS 1624 (Strauss et al. 1999), for example, does not have a hot companion, yet shows no flux blueward of 0.8 μm, indicating a strong absorption in the optical, as does Gl229B. This suggests that the source of absorption is a common atmospheric BD property, precluding the haze opacity scenario. Strong alkali resonance lines (K I, Na I) have been proposed recently as an alternative, or complementary solution (Tsuji et al. 1999; Burrows et al. 1999). Clearly this question is not settled yet and requires futher observational tests and consistent calculations.

For $(J-K) \sim$ 1.0-1.9, good agreement is found between the data and the DUSTY models (see Figure 6), except for the L0-dwarf 2MASS-WJ0746425+200032 (Reid et al. 1999) ($M_{\rm K}$=9.70, J-K=1.25), which lies significantly above both the other data and the models, making it a probable unresolved binary, as suggested by these authors.

An interesting feature of this diagram is a hint that the redder L-dwarfs of Dahn et al. (2000), and the slope of the observed L-dwarf sequence itself, seem to deviate from the DUSTY tracks for $M_{\rm K} \gtrsim 11.5$ and $(J-K) \gtrsim 1.5$, the reddest observed objects having a color $(J-K) \sim 1.9$, i.e. $T_{\rm eff} \sim 1800$ K. If the parallax and the photometry of these objects are confirmed, this may very well illustrate gravitational settling of some grains below the photosphere for these objects, as mentioned in §2.1. This will yield less backwarming and thus progressively cooler atmospheres (see Figure 1), increasing H_2O, CO and H2 absorption in the IR. Once CH_4 forms near the photosphere, the integrated flux over the K-band is strongly reduced, although the flux still peaks around 1 μm, leading to Gl229B-like colors. Whether this transition occurs sharply or smoothly remains to be elucidated. Note that the CO-CH_4 transition occurs gradually with some of the two elements being present in the stability field of the other so that cool stars do contain some limited amount of methane and CO has been detected in Gl229B (Noll et al. 1997; Oppenheimer et al. 1998). The recently discovered methane-dwarfs (Burgasser et al. 1999), unfortunately, do not bring information about this transition because of their color selection criterium, $J - K < 0.4$. In case of an abrupt change in color between "L" and "methane"-dwarfs, there should be indeed a "no-BD land" in the region $0.5 \lesssim J - K \lesssim 1.0$ with a sharp transition for $T_{\rm eff} \sim T_{\rm gas} = 1300 - 1400$ K, the temperature of formation of methane in the $P \approx 3 - 10$ bar range. This corresponds to masses $m \approx 0.015 - 0.02\, M_\odot$ for t=0.1 Gyr, $m \approx 0.045 - 0.05\, M_\odot$ for t=1 Gyr and $m \approx 0.065\, M_\odot$ for t=5 Gyr. In any events, this concerns objects cooler than $T_{\rm eff} \approx$ 1700-1800 K, the temperature derived with the DUSTY models along the 1 Gyr isochrone for LHS102B (Goldman et al. 1999; see also Figure 6), the reddest L-dwarf with known parallax, and for 2MASS-W1632+19, the faintest L-dwarf in the Dahn et al. (2000) sample with $M_{\rm K} \sim 12.75$, $(J - K) \sim 1.9$. These temperatures agree within 100 K with the ones derived spectroscopically by Basri et al. (1999) based on alkali resonance absorption lines in the optical spectrum. Objects cooler than 2MASS-W1632+19 thus correspond to BDs with masses $m \lesssim 0.03\ M_\odot$ for ages $t > 0.1$ Gyr, $m \lesssim 0.06\ M_\odot$ for $t > 1$ Gyr and to essentially *all* BDs for $t \gtrsim 2.5$ Gyr (see Figure 2).

The same general behavior as in $(J - K)$ is found in $(J - H)$, with the same color saturation observed for the reddest L dwarfs for $M_{\rm J} \gtrsim 13$ and $(J - H) \lesssim 1.2$. Although not shown in the present paper, a COND isochrone at $t \sim$(a few)$\times 10^8$ yr fits well GL229B both in $(J-H)$, in contrast to Burrows et al. (1997) models, and $(J-K)$ colors. Their models could not reproduce the L'-band of GL229B. Since then, Leggett et al. (1999) revised the flux of GL229B, with a significant modification of the L' band, which is now reproduced by the Burrows et al. (1997) models. The reason of their poor fit in the H-band, however, compared with the present models, remains unclear. Indeed the explanation proposed in Burrows et al. (1997) was based on previous, less accurate observations of Gl229B, as mentioned above, and does not hold anymore.

Finally, Figure 7 displays L' versus $(K-L')$. The K band is affected by H_2, H_2O and CH_4 absorption, whereas the L' is strongly affected by methane (Allard et al. 1996; Marley et al. 1996; Tsuji et al. 1996). The trends displayed in the previous IR diagrams are replicated, with a severe reddening due to grain backwarming effects in the DUSTY models, but also a substantial reddening for the COND and grainless model, due to the strong CH_4 absorption in the K-band.

The magnitudes of brown dwarfs and very-low-mass stars with dusty atmospheres for several isochrones are displayed in Tables 1-5. We stress, however, that the flux for these objects peaks around 1 μm, so that J,Z and H remain the most favorable bands for detection.

*** FIGURE 7 ***

4. Discussion and conclusion

The comparisons in various CMDs displayed in the previous section illustrate the good general agreement between the present theory of evolution of very-low-mass stars and brown dwarfs with dusty atmospheres and observations. The models which include grain formation *and* opacity in the atmosphere explain successfully the IR colors of late M- and L-dwarfs, as well as their blue loop in the optical, although improvement is still needed for the latter case to reach accurate quantitative agreement with observations. As shown by Kirkpatrick et al. (1999a) for GD165B and Ruiz et al. (1997) for Kelu-1, the DUSTY models improve also significantly the agreement with observed IR spectra. The present models provide a consistent description of the physics going on in the interior and the atmosphere of objects at the bottom of and below the main sequence, from M-dwarfs to L-dwarfs. They can be used with reasonable confidence in the IR bands ($JKL'M$) to calibrate the main properties, mass, age, $T_{\rm eff}$, L of identified late-M and L-dwarfs. Shortcomings still appear in the optical, whatever the treatment of dust, in spite of noticeable improvement (see Figure 4). Baraffe et al. (1998) already pointed out a possible missing source of opacity in the optical to explain the observed $(V-I)$ colors of M-dwarfs between $T_{\rm eff} \sim 3600$ K and ~ 2300 K. Although the new TiO linelist from AMES (Schwenke, 1998) improves appreciably the situation (see Figure 4), a $\sim 0.2-0.3$ mag discrepancy still remains with observations (see Figure 5). Below ~ 2300 K, comparison of the DUSTY models with observations in $(V-I)$ (see Figure 4) strongly suggests either an underestimate of optical opacities or an underestimate of the depletion of molecular absorbers during grain condensation. Problems appear as well in spectroscopic analysis of atomic line profiles where the DUSTY models cannot match the optical observations (Tinney et al. 1998; Basri et al. 1999). Another remaining caveat of the present theory arises from shortcomings in the absorption coefficients of water, yielding a ~ 0.2 mag offset in $(J-K)$ for $T_{\rm eff} \gtrsim 2300$ K when using the most recent H_2O line list (see e.g. Figure 6). Finally, the optical spectrum of GL229B remains to be described accurately. Present COND synthetic spectra overestimate the optical flux, pointing out a missing source of opacity. Work in this direction is under progress.

Although it is important to solve these problems and eliminate these shortcomings, it is obvious from the various CMDs that substellar objects must be searched in the near-infrared. Brown dwarfs around 1500 K radiate more than 90% of their energy at wavelengths longward of 1 μm. The flux peaks at 1.1 and 1.3 μm, and J, Z, H are the favored broadband filters for detection. It is thus reinsuring, given the complexity of the underlying physics, that the present models of dusty substellar objects describe the observations in near-IR bands with reasonable success.

If dust formation and absorption successfully explain the transition between M- and L-dwarfs, a theoretical and observational gap still exists between L- and methane-dwarfs. Models including dust opacity reach rapidly very red IR colors $(J-K) > 2$, whereas observations of the reddest or faintest L dwarfs show a saturation of their $(J-K)$ and $(J-H)$ colors at 1.9 and 1.2 respectively, which corresponds to $T_{\rm eff} \sim$ 1700-1800 K (see Figure 6). This very likely illustrates ongoing dynamical processes near the photosphere. As outlined in §2.1, the proximity of the top of the convection zone from the photosphere may induce turbulent mixing and prevent the grains to diffuse downward. As convection retreats to deeper layers for cooler objects, gravitational settling of condensed species may lead to cooler atmospheres, because of the decreasing opacity, with a transition to very blue near infrared colors once methane forms near the photosphere. These dynamical processes of grain formation and diffusion are not included in the theory yet and represent indeed the next major challenge. Theory definitely needs some guidance from observations through this puzzle, by getting spectra, parallaxes and photometry of the coolest L-dwarfs and by either filling or confirming the presently expected brown dwarf dearth between the coolest L-dwarfs and the hottest methane dwarfs around $T_{\rm eff} \approx 1300-1400$ K.

Note: Various isochrones for the DUSTY models from 10^7 yr to 10^{10} yr, covering a range of mass from 0.01 $M_\odot$ to 0.1 $M_\odot$ and $T_{\rm eff}$ from 900K to 3000K are available by anonymous ftp (same format as Table 1):

ftp ftp.ens-lyon.fr

username: anonymous

ftp > cd /pub/users/CRAL/ibaraffe

ftp > get DUSTY00_models

ftp > quit

Note that the DUSTY models are given in the Tables down to $T_{\rm eff}$=900K, but this limit is clearly unrealistic for dusty atmospheres, as seen in the various figures of the paper.

Special requests for models in any particular filters can be addressed to I. Baraffe.

We are very grateful to C. Dahn and H. Harris for providing data prior to publication and to A. Potekhin for providing the conductive opacities. We are also thankful to E. Martín and to the referee, D. Saumon, for constructive suggestions and comments. Part of this work was performed at the AAO (Sidney) under the auspice of the franco-australian cooperation program in Astronomy (CNRS/ARC). G.C and I.B are very indebted to B. Boyle, C. Tinney and the staff of the AAO for their generous hospitality during this visit.

This work was supported in part by a CNRS-NSF "dark matter" grant, NSF grant AST-9720704, NASA ATP grant NAG 5-3018 and LTSA grant NAG 5-3619 to the University of Georgia, and NASA LTSA grant NAG5-3435 to Wichita State University. The computations were done at the Pôle Scientifique de Modélisation Numérique at ENS-Lyon, on the T3E of Centre d'Etudes Nucléaires de Grenoble, on the IBM SP2 of CNUSC, the SGI Origin 2000 of the UGA UCNS, on the IBM SP2 of the San Diego Supercomputer Center (SDSC) with support from the National Science Foundation, and on the Cray T3E of the NERSC with support from the DoE. We thank all these institutions for a generous allocation of computer time.

REFERENCES

Alexander D.R, Fergusson J.W., 1994, ApJ, 437, 879

Allard F., 1998, In Brown dwarfs and extrasolar planets, ASP conf. Series, 134, p. 370

Allard F., 1999, In Very Low-Mass Stars and Brown Dwarfs in Stellar Clusters and Associations. Proc. Euroconference, La Palma, in press

Allard F., Hauschildt P.H., 1995, ApJ, 445, 433

Allard F., Hauschildt P.H., Baraffe I., Chabrier G., 1996, ApJ, 465, L123

Allard F., Hauschildt P.H., Alexander D.R., Starrfield S., 1997, ARA&A, 35, 137

Allard F., Hauschildt P.H., Alexander D.R., Tamanai A., Ferguson J., 2000a, ApJ, in preparation

Allard F., Hauschildt P.H., Schwenke, D., 2000b, ApJ, submitted

Baraffe I., Chabrier G., 1996, ApJ, 461, L51

Baraffe I., Chabrier G., Allard F., Hauschildt P.H., 1997, A&A 327, 1054

Baraffe I., Chabrier G., Allard F., Hauschildt P.H., 1998, A&A, 337, 403, BCAH98

Basri G., Mohanty S., Allard F., et al. 1999, ApJ, in press

Bessell M. S., 1990, PASP, 102, 1181

Bouvier J., Stauffer J.R., Martín E.L., Barrado y Navascues D., Wallace B., et al. 1998, A&A, 336, 490

Brassard P., Fontaine G., 1994, In The equation of state in astrophysics, IAU colloquium, 147, p. 560

Burgasser A.J., Kirkpatrick J.D., Brown M.E., et al. 1999, ApJ, 422, L65

Burrows A., Liebert J., 1993. Rev. Mod. Phys., 65, 301

Burrows A., Hubbard W.B., Saumon D., Lunine J. I., 1993, ApJ, 406, 158

Burrows A., Marley M., Hubbard W.B., et al. 1997, ApJ, 491, 856

Burrows A., Marley M., Sharp C.M., 1999, ApJ, submitted

Burrows A., Sharp C.M,. 1999. ApJ, 512, 843

Chabrier G., Baraffe I., Plez B., 1996, ApJ, 459, L91

Chabrier G., Baraffe I., 1997, A&A 327, 1039, CB97

Chabrier G., Baraffe I., 2000, ARA&A, in press

Cuby J.G., Saracco P., Moorwood A.F.M., et al.. 1999. A&A, 349, L41

Dahn C.C., Liebert J., Harris H.C., Guetter H.H., 1995, in The bottom of the main sequence and below, ed. C. Tinney, Springer Verlag, p.239

Dahn C.C., Guetter H.H., Harris H.C., Henden A.A., Luginbuhl C.B., et al. 2000, in From Giant Planets to Cool Stars, Flagstaff, 1999

Delfosse X., Tinney C.G., Forveille T., Epchtein N., Borsenberger J., et al., 1999, A&AS, 135, 41

Fegley B., Lodders K., 1994, Icarus 110, 117

Fegley B., Lodders K., 1996, ApJ, 472, L37

Goldman B., Delfosse X., Forveille T., Afonso C., Alard C., et al. 1999, A&A, 351, L5

Golimowski D.A., Burrows C.J., Kulkarni S.R., Oppenheimer B.R., Brukardt R.A., 1998, AJ, 115, 2579

Griffith C.A., Yelle R.V., Marley M.S., 1998, Science, 282, 2063

Grossman L., 1972, GeCoA, 38, 47

Hauschildt P.H., Allard F., Baron E., 1999, ApJ, 512, 377, HAB99

Hubbard W.B., Lampe M., 1969, ApJS, 18, 297

Itoh N., Mitake S., Iyetomi H., Ichimaru S., 1983, ApJ, 273, 774

Jørgensen U. G., 1994, ApJ, 284, 179

Jones H.R.A., Tsuji T., 1997, ApJ, 480, L39

Kirkpatrick J.D., Allard F., Bida T., et al. 1999a, ApJ, 519, 834

Kirkpatrick J.D., Reid N.I., Liebert J., et al. 1999b, ApJ, 519, 802

Koerner, D. W., Kirkpatrick, J. D., McElwain, M. W. & Bonaventura, N. R., 1999, ApJ, 526, L25

Leggett S.K., 1992, ApJS, 82, 351

Leggett S.K., Allard F., Hauschildt P.H., 1998, ApJ, 509, 836

Leggett S.K., Toomey D.W., Geballe T.R., Brown R.H., 1999, ApJ, 517, L139

Lodders K., 1999, ApJ, 519, L793

Lunine J.I., Hubbard W.B., Burrows A., Wang Y-P., Garlow K., 1989, ApJ, 338, 314

Marley M.S., Saumon D., Guillot T., et al. 1996, Science, 272, 1919

Martín, E. L., Brandner, W. & Basri, G. 1999, Science, 283, 1718

Martín E.L., Delfosse X., Basri G., Goldman B., Forveille T., & Zapatero Osorio, M. R. 1999, AJ, 118, 2466

Miller S., Tennyson J., Jones H.R.A, Longmor, A.J., 1994, in Molecules in the Stellar Environment, ed. U.G Jorgensen, Lecture Notes in Physics

Mitake S., Ichimaru S., Itoh N., 1984, ApJ, 277, 375

Monet, D. G., Dahn C. C., Vrba F. J., Harris H. C., Pier J. R., Luginbuhl C. B., Ables H., D., 1992, AJ, 103, 638

Noll, K.S., Geballe, T.R., Marley, M.S., 1997, ApJ, 489, L87

Oppenheimer B.R., Kulkarni S.R., Matthews K., Nakajima T., 1995, Science, 270, 1478

Oppenheimer B.R., Kulkarni S.R., Matthews K., Van Kerkwijk M.H., 1998, ApJ, 502, 932

Partridge, H., and Schwenke, D.W., 1997, *J. Chem. Phys.*, 106, 4618

Potekhin, A.Y., Baiko, D.A., Haensel, P., Yakovlev, D.G., 1999, A&A, 346, 345

Reid N., Kirkpatrick J.D., Gizis J.E., Dahn C.C., Monet D.G., et al. 1999, AJ, in press, astro-ph/9909336

Rossow W.B., 1978, Icarus, 36,1

Ruiz M., Leggett S.K., Allard F., 1997, ApJ, 491, L107

Saumon D., Hubbard W.B., Burrows A., Guillot T., Lunine J.I., Chabrier, G., 1996, ApJ, 460, 993

Schwenke, D.W., 1998, *Chemistry and Physics of Molecules and Grains in Space*, Faraday Discussion 109, 321

Skrutskie M.F., Schneider S.E., Stiening R., et al. 1997, in The Impact of Large Scale Near IR sky Surveys, ed. F. Garzon et al. Kluwer:Dordrecht, p. 25

Strauss M.A., Fan X., Gunn J.E., et al. 1999, ApJ, 522, L61

Tinney C.G., Delfosse X., Forveille T., Allard F., 1998, A&A, 338, 1066

Tsuji T., Ohnaka K., Aoki W., Nakajima, T., 1996, A&A, 308, L29

Tsuji T., Ohnaka K., Aoki W., 1999, A&A, 520, L119

This manuscript was prepared with the AAS LaTeX macros v4.0.

Table 1: DUSTY model isochrone for 0.1 Gyr. T_{eff} is in K, the gravity g in cgs. The lithium abundance is normalized to the initial abundance, which is $X_{Li_0} = 10^{-9}$ by mass fraction in the present calculations. The VRI magnitudes are in the Johnson-Cousins system (Bessell 1990), JHK in the CIT system (Leggett 1992), L′ in the Johnson-Glass system and M in the Johnson system.

$m/M_\odot$	T_{eff}	$\log L/L_\odot$	$\log g$	$R/R_\odot$	Li/Li$_0$	M_V	M_R	M_I	M_J	M_K	$M_{L'}$	M_M
0.010	916.	-4.98	4.21	0.130	1.0000	42.64	35.06	31.45	22.06	15.20	11.71	11.30
0.012	1333.	-4.25	4.22	0.141	1.0000	29.33	24.92	22.13	16.50	12.14	10.10	10.12
0.015	1290.	-4.37	4.37	0.132	1.0000	30.63	25.96	23.08	17.14	12.52	10.32	10.36
0.020	1441.	-4.21	4.53	0.127	1.0000	27.30	23.35	20.73	15.68	11.86	10.14	10.20
0.030	1878.	-3.75	4.71	0.127	1.0000	21.21	18.37	15.96	12.22	10.76	9.74	9.89
0.040	2234.	-3.41	4.80	0.132	1.0000	18.72	16.41	13.95	11.04	10.16	9.37	9.62
0.050	2483.	-3.18	4.84	0.140	0.9990	17.07	15.14	12.86	10.47	9.70	9.04	9.28
0.055	2576.	-3.09	4.86	0.145	0.9920	16.44	14.65	12.48	10.27	9.51	8.90	9.12
0.060	2652.	-3.01	4.87	0.149	0.9630	15.95	14.26	12.18	10.11	9.36	8.77	8.98
0.070*	2768.	-2.88	4.88	0.159	0.6680	15.19	13.64	11.70	9.83	9.09	8.55	8.72
0.072	2787.	-2.86	4.88	0.161	0.5380	15.07	13.54	11.63	9.78	9.04	8.51	8.68
0.075	2814.	-2.83	4.88	0.164	0.3290	14.89	13.40	11.52	9.71	8.97	8.45	8.62
0.080	2854.	-2.78	4.89	0.169	0.0664	14.65	13.19	11.36	9.61	8.87	8.36	8.52
0.090	2920.	-2.69	4.89	0.178	0.0000	14.23	12.84	11.09	9.41	8.68	8.20	8.34
0.100	2971.	-2.63	4.90	0.185	0.0000	13.92	12.58	10.89	9.27	8.54	8.07	8.21

* HBMM

Table 2: Same as Table 1 for 0.5 Gyr

$m/M_\odot$	T_{eff}	$\log L/L_\odot$	log g	$R/R_\odot$	Li/Li$_0$	M_V	M_R	M_I	M_J	M_K	$M_{L'}$	M_M
0.020	901.	-5.14	4.65	0.111	1.0000	43.80	35.89	32.23	22.56	15.59	12.11	11.67
0.030	1170.	-4.73	4.86	0.106	1.0000	33.93	28.57	25.49	18.78	13.65	11.09	11.10
0.040	1461.	-4.36	5.01	0.104	1.0000	27.41	23.50	20.90	15.94	12.20	10.51	10.62
0.050	1751.	-4.06	5.11	0.103	0.9540	22.45	19.47	17.10	13.18	11.35	10.23	10.36
0.055	1902.	-3.91	5.15	0.103	0.5610	21.42	18.64	16.25	12.60	11.20	10.16	10.32
0.060	2048.	-3.78	5.19	0.104	0.0069	20.56	17.91	15.46	12.12	11.00	10.04	10.25
0.070*	2295.	-3.56	5.23	0.106	0.0000	18.95	16.62	14.18	11.42	10.58	9.78	10.06
0.072	2332.	-3.52	5.24	0.107	0.0000	18.71	16.44	14.01	11.34	10.51	9.74	10.02
0.075	2400.	-3.46	5.24	0.108	0.0000	18.26	16.09	13.71	11.18	10.39	9.65	9.93
0.080	2505.	-3.37	5.25	0.111	0.0000	17.56	15.56	13.27	10.95	10.18	9.51	9.79
0.090	2678.	-3.19	5.24	0.118	0.0000	16.40	14.67	12.58	10.57	9.83	9.24	9.48
0.100	2809.	-3.05	5.23	0.128	0.0000	15.52	13.97	12.06	10.25	9.52	8.99	9.19

* HBMM

Table 3: Same as Table 1 for 1 Gyr

$m/M_\odot$	T_{eff}	$\log L/L_\odot$	log g	$R/R_\odot$	Li/Li$_0$	M_V	M_R	M_I	M_J	M_K	$M_{L'}$	M_M
0.030	958.	-5.11	4.90	0.102	1.0000	40.76	33.66	30.17	21.50	15.22	11.98	11.68
0.040	1189.	-4.77	5.06	0.098	1.0000	33.53	28.29	25.25	18.69	13.69	11.20	11.24
0.050	1424.	-4.48	5.18	0.096	0.9320	28.26	24.20	21.54	16.42	12.53	10.74	10.86
0.055	1550.	-4.34	5.22	0.095	0.3790	26.08	22.48	20.00	15.39	12.08	10.59	10.71
0.060	1675.	-4.21	5.27	0.094	0.0000	23.95	20.72	18.33	14.14	11.71	10.48	10.59
0.070*	2012.	-3.88	5.32	0.096	0.0000	21.10	18.37	15.95	12.47	11.24	10.24	10.43
0.072	2089.	-3.80	5.32	0.097	0.0000	20.51	17.87	15.41	12.17	11.10	10.15	10.37
0.075	2185.	-3.71	5.33	0.098	0.0000	19.82	17.32	14.85	11.85	10.92	10.03	10.29
0.080	2358.	-3.54	5.32	0.103	0.0000	18.66	16.41	14.00	11.38	10.57	9.80	10.08
0.090	2625.	-3.27	5.28	0.113	0.0000	16.81	14.99	12.84	10.74	9.99	9.38	9.64
0.100	2790.	-3.08	5.25	0.125	0.0000	15.68	14.10	12.16	10.33	9.59	9.05	9.26

* HBMM

Table 4: Same as Table 1 for 5 Gyr

$m/M_\odot$	T_{eff}	$\log L/L_\odot$	log g	$R/R_\odot$	Li/Li$_0$	M_V	M_R	M_I	M_J	M_K	$M_{L'}$	M_M
0.050	907.	-5.35	5.26	0.086	0.9210	43.03	35.38	31.77	22.53	15.95	12.57	12.11
0.055	990.	-5.21	5.32	0.085	0.2840	39.43	32.76	29.36	21.21	15.26	12.23	11.95
0.060	1097.	-5.04	5.37	0.084	0.0000	35.60	29.92	26.76	19.74	14.50	11.81	11.74
0.070*	1593.	-4.36	5.40	0.087	0.0000	25.54	22.08	19.67	15.23	12.13	10.73	10.84
0.072	1754.	-4.18	5.40	0.089	0.0000	22.96	19.93	17.58	13.63	11.68	10.54	10.66
0.075	1998.	-3.92	5.38	0.092	0.0000	21.31	18.55	16.14	12.62	11.35	10.32	10.50
0.080	2295.	-3.61	5.34	0.100	0.0000	19.12	16.77	14.32	11.57	10.73	9.91	10.20
0.090	2621.	-3.28	5.29	0.113	0.0000	16.85	15.02	12.86	10.75	10.01	9.39	9.65
0.100	2791.	-3.08	5.25	0.124	0.0000	15.68	14.10	12.16	10.33	9.59	9.05	9.26

* HBMM

Table 5: Same as Table 1 for 10 Gyr

$m/M_\odot$	T_{eff}	$\log L/L_\odot$	log g	$R/R_\odot$	Li/Li$_0$	M_V	M_R	M_I	M_J	M_K	$M_{L'}$	M_M
0.060	971.	-5.29	5.40	0.081	0.0000	40.34	33.44	30.00	21.61	15.52	12.43	12.09
0.070*	1552.	-4.42	5.41	0.086	0.0000	26.27	22.67	20.19	15.60	12.28	10.79	10.91
0.072	1744.	-4.19	5.40	0.089	0.0000	23.10	20.05	17.69	13.71	11.70	10.55	10.67
0.075	1998.	-3.92	5.38	0.092	0.0000	21.31	18.55	16.14	12.62	11.35	10.32	10.50
0.080	2297.	-3.61	5.34	0.100	0.0000	19.11	16.76	14.31	11.56	10.72	9.91	10.20
0.090	2622.	-3.27	5.29	0.113	0.0000	16.84	15.01	12.85	10.75	10.01	9.39	9.65
0.100	2793.	-3.08	5.25	0.124	0.0000	15.66	14.09	12.15	10.33	9.59	9.05	9.26

* HBMM

FIGURE CAPTIONS

Fig. 1.— Atmosphere profiles for $T_{\rm eff}$=1800 K and log g=5. Different treatments of dust are considered. Solid line (full circle): DUSTY; long-dashed line (full square): COND; dash-dotted line (open circle): NextGen (see text). The photosphere ($\tau_{\rm Rosseland} \sim 1$) is located at $T \sim 2100$ K for all models, whereas the end of the curves correspond to $\tau = 100$, the boundary condition with the interior profile. The symbols on each curve indicate the onset of convection

Fig. 2.— Evolution of $T_{\rm eff}$ as a function of time (in yr) for different masses and atmosphere models. Solid lines: DUSTY; long-dashed lines: COND; dash-dotted lines: NextGen. Masses are indicated in $M_\odot$

Fig. 3.— Evolution of the conductive core $M_{\rm cond}/M_{\rm tot}$ (shaded area) as a function of time for a 0.06 $M_\odot$ brown dwarf.

Fig. 4.— CMD for the optical colors $(V-I)$ at the bottom of the Main Sequence and below. The data is from Monet et al. (1992) (filled circles), Dahn et al. (1995) (crosses), Dahn et al. (2000) (filled squares) and Reid et al. (1999) (filled triangles). Kelu-1 (Ruiz et al. 1997) is indicated by a full diamond. Theoretical models correspond to various isochrones: short-dashed and solid lines: DUSTY models for 0.1 and 1 Gyr respectively; long-dashed line: COND models for 1 Gyr; dash-dotted line: NextGen models for 1 Gyr. Masses (in $M_\odot$) and $T_{\rm eff}$ are indicated on the 1 Gyr DUSTY isochrone by open circles. The COND models go from 0.08 $M_\odot$ (same as DUSTY) to 0.03 $M_\odot$. See Tables 1-5 for the location of the HBMM at different ages

Fig. 5.— CMD for the optical color $(R - I)$. The filled circles are the Pleiades data from Bouvier et al. (1998). The other symbols and the models are the same as in Figure 4. See Tables 1-5 for the location of the HBMM at different ages

Fig. 6.— CMD for the near-IR color $(J-K)$. The dots are the data from Leggett (1992). The other symbols are the same as in Figure 4. Some identified BDs are indicated by diamonds: Kelu-1 (Ruiz et al. 1997); GD165B (Kirkpatrick et al. 1999a); LHS102B (Goldman et al. 1999). Theoretical models are the same as in Fig 4. Crosses on the COND track indicate masses in $M_{\odot}$ and $T_{\rm eff}$ in K. See Tables 1-5 for the location of the HBMM at different ages

Fig. 7.— CMD for the IR color $(K-L')$. The dots are data from Leggett (1992). Theoretical models are the same as in Figure 6, with the same masses indicated on the COND isochrone (long-dash line, $\times$). The dotted curve corresponds to the DUSTY isochrone for 10 Gyr. Masses in $M_{\odot}$ are indicated on the DUSTY isochrone for 1 Gyr (solid line, O); $T_{\rm eff}$ for $m \geq 0.08 M_{\odot}$ are the same as in Figure 4. See Tables 1-5 for the location of the HBMM at different ages

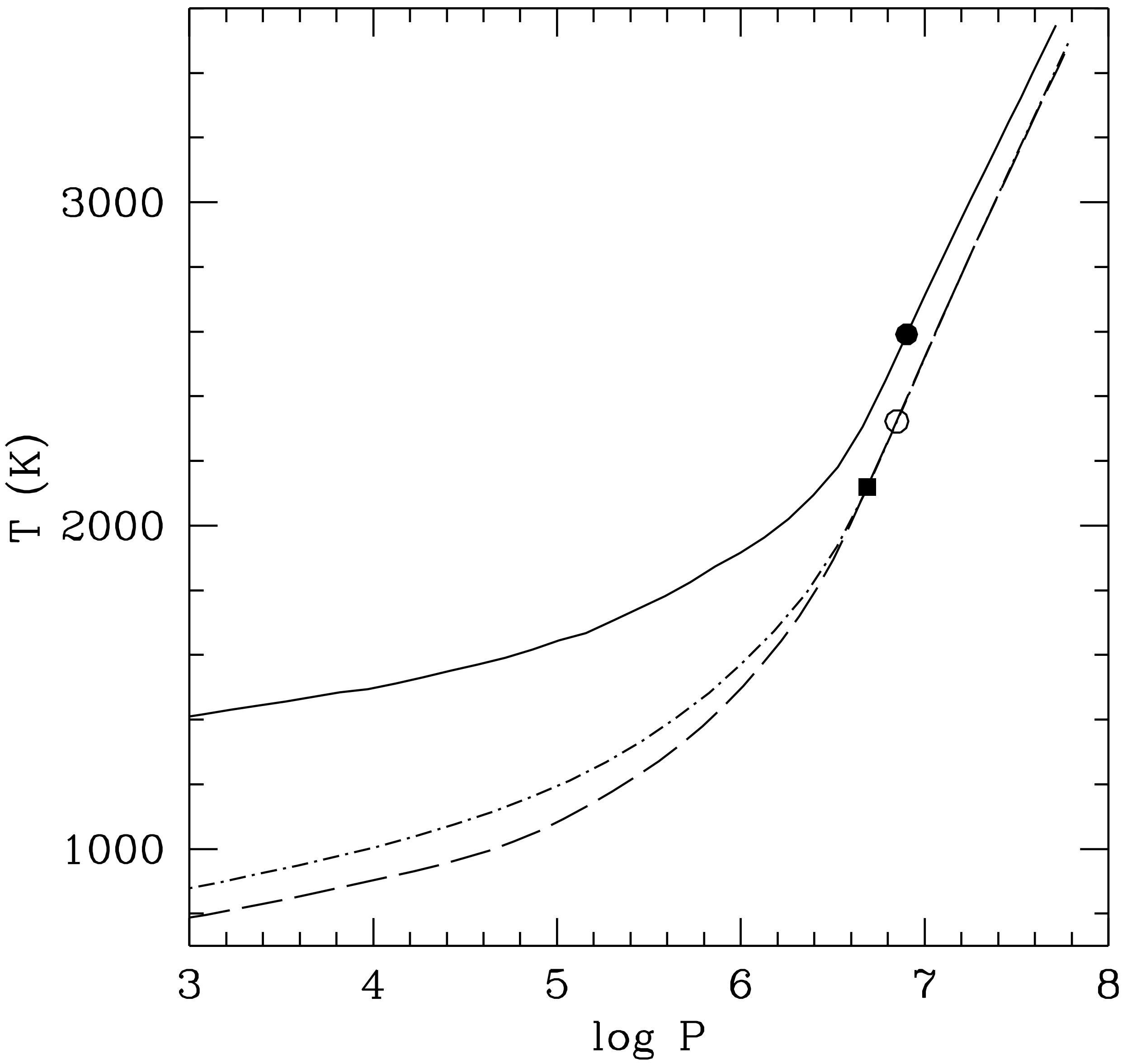
3000
2000
1000
T (K)
3
4
5
6
7
8
log P

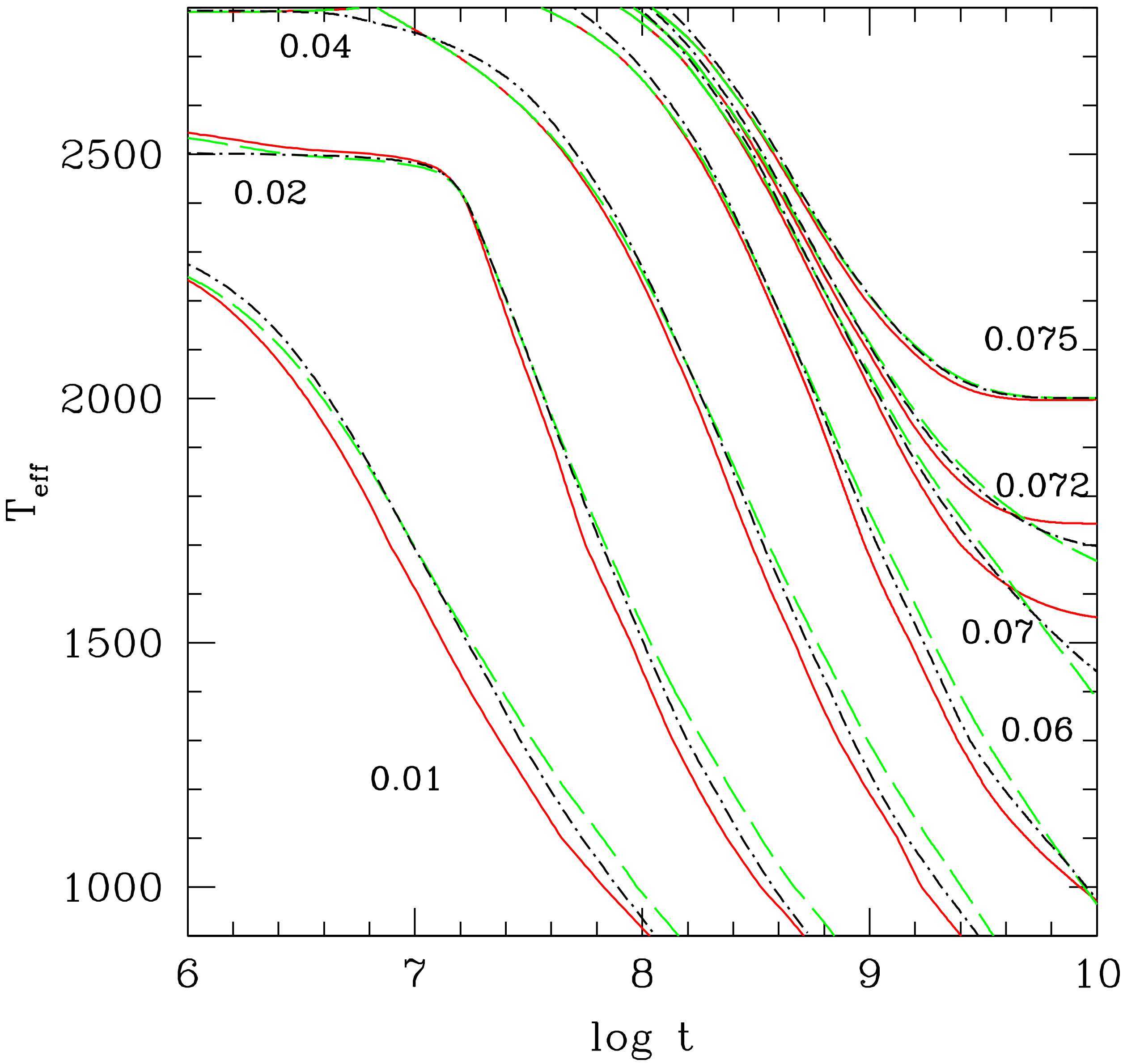
0.04
0.02
0.01
0.075
0.072
0.07
0.06
2500
2000
1500
1000
T_{eff}
6
7
8
9
10
log t

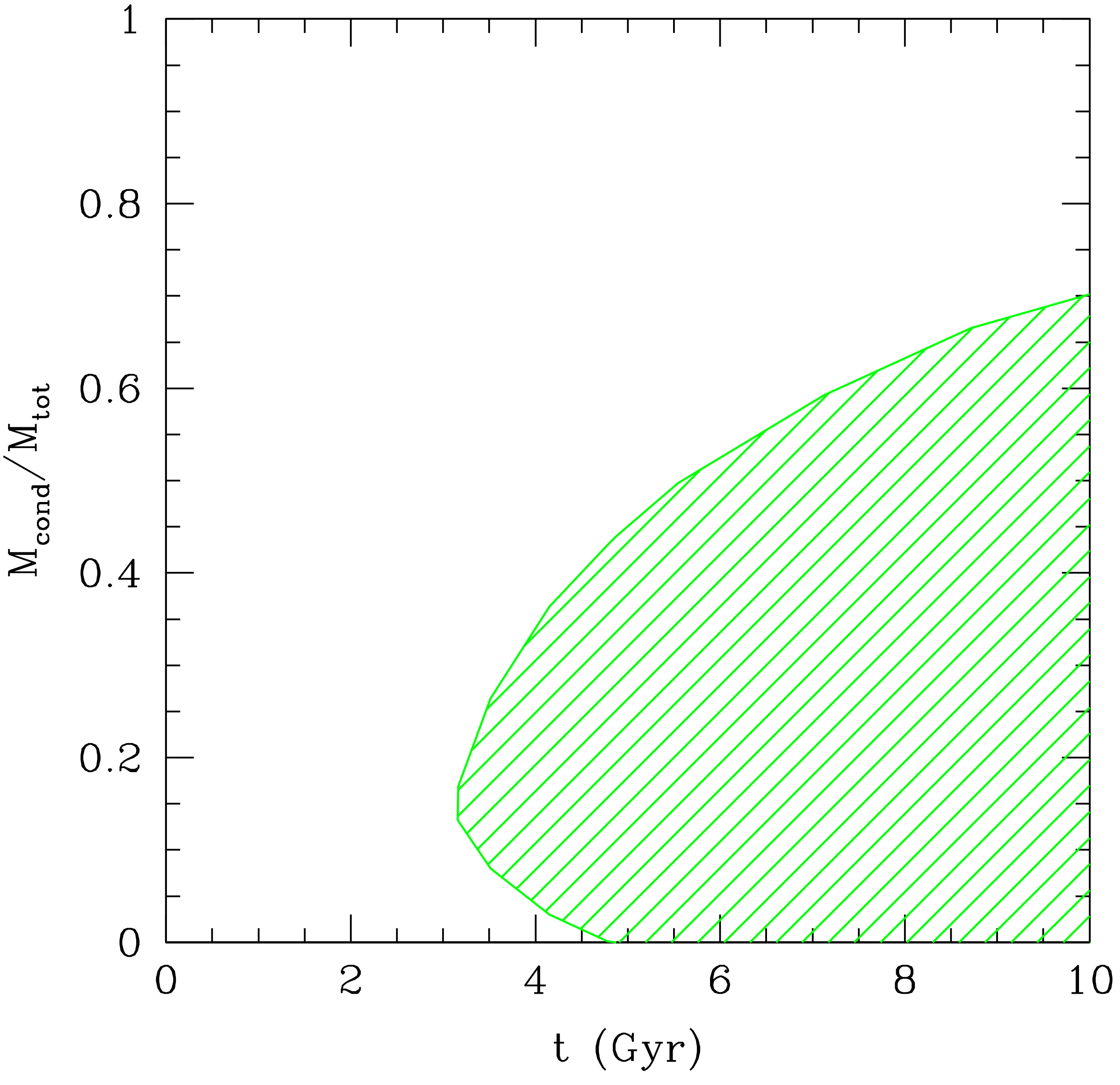

1
0.8
0.6
0.4
0.2
0
M_{cond}/M_{tot}
0
2
4
6
8
10
t (Gyr)

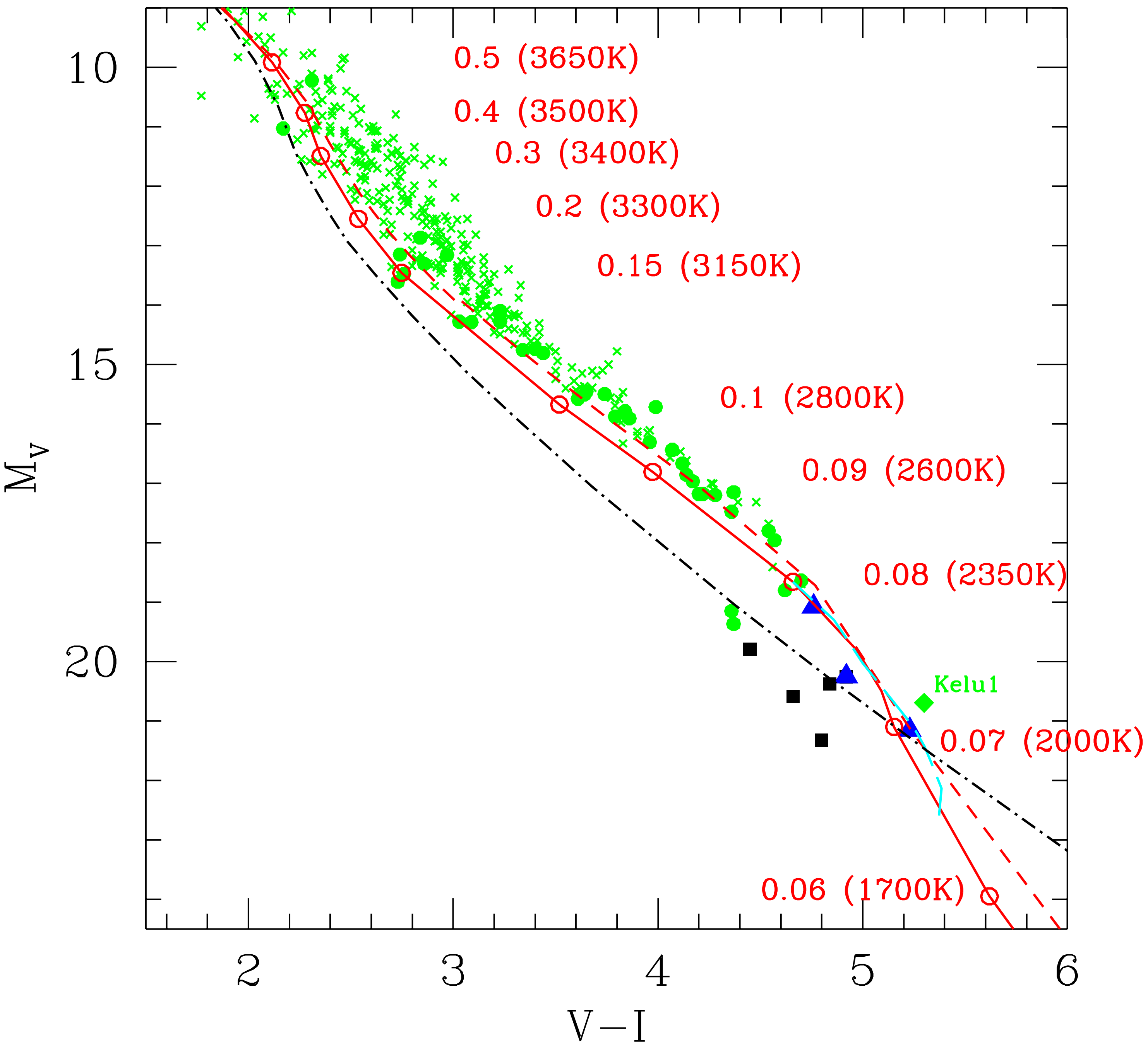
0.5 (3650K)
0.4 (3500K)
0.3 (3400K)
0.2 (3300K)
0.15 (3150K)
0.1 (2800K)
0.09 (2600K)
0.08 (2350K)
Kelu1
0.07 (2000K)
0.06 (1700K)
10
15
20
M_V
2
3
4
5
6
V−I

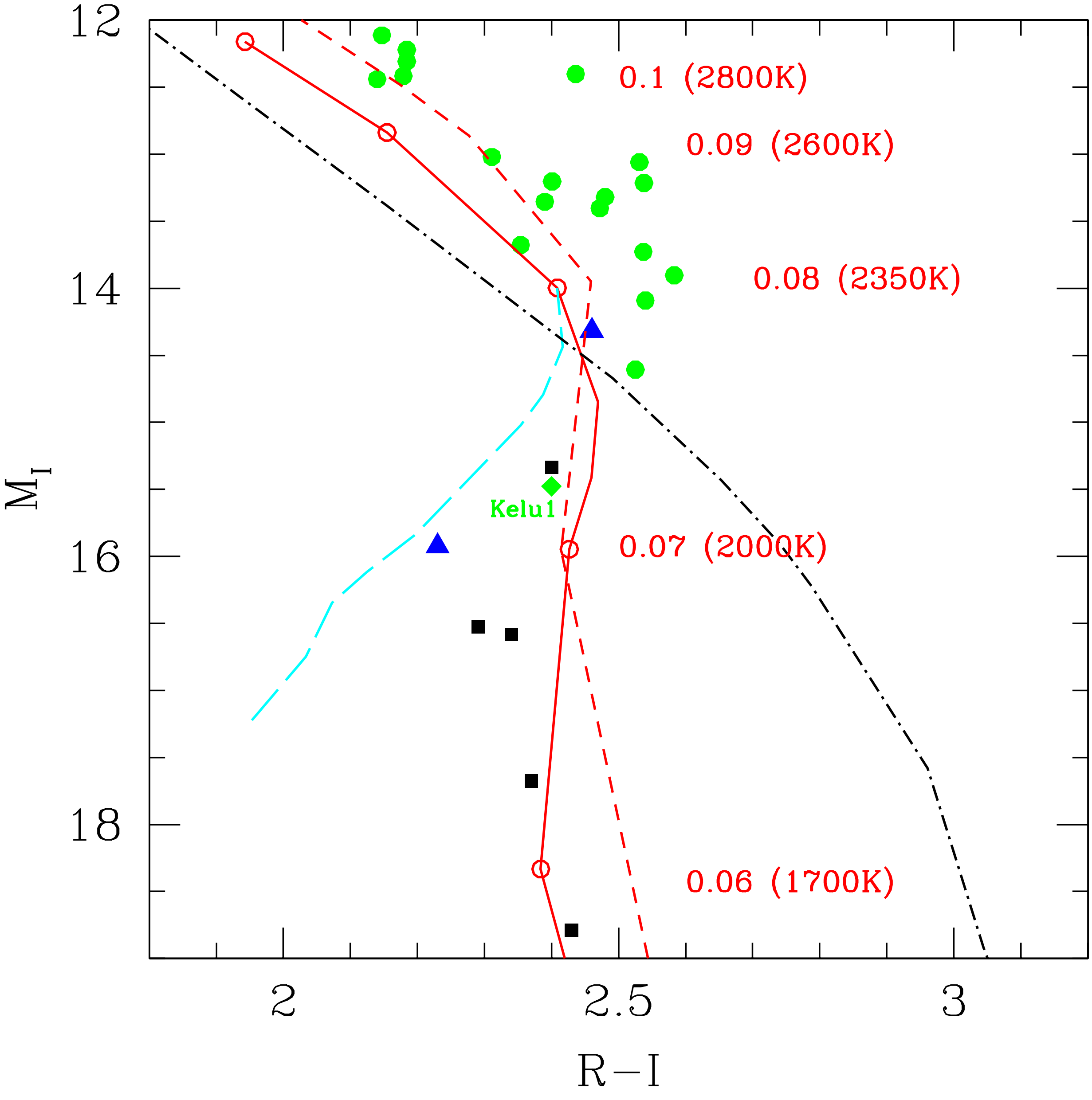
12
14
16
18
2
2.5
3
R−I
M_I
0.1 (2800K)
0.09 (2600K)
0.08 (2350K)
0.07 (2000K)
0.06 (1700K)
Kelu1

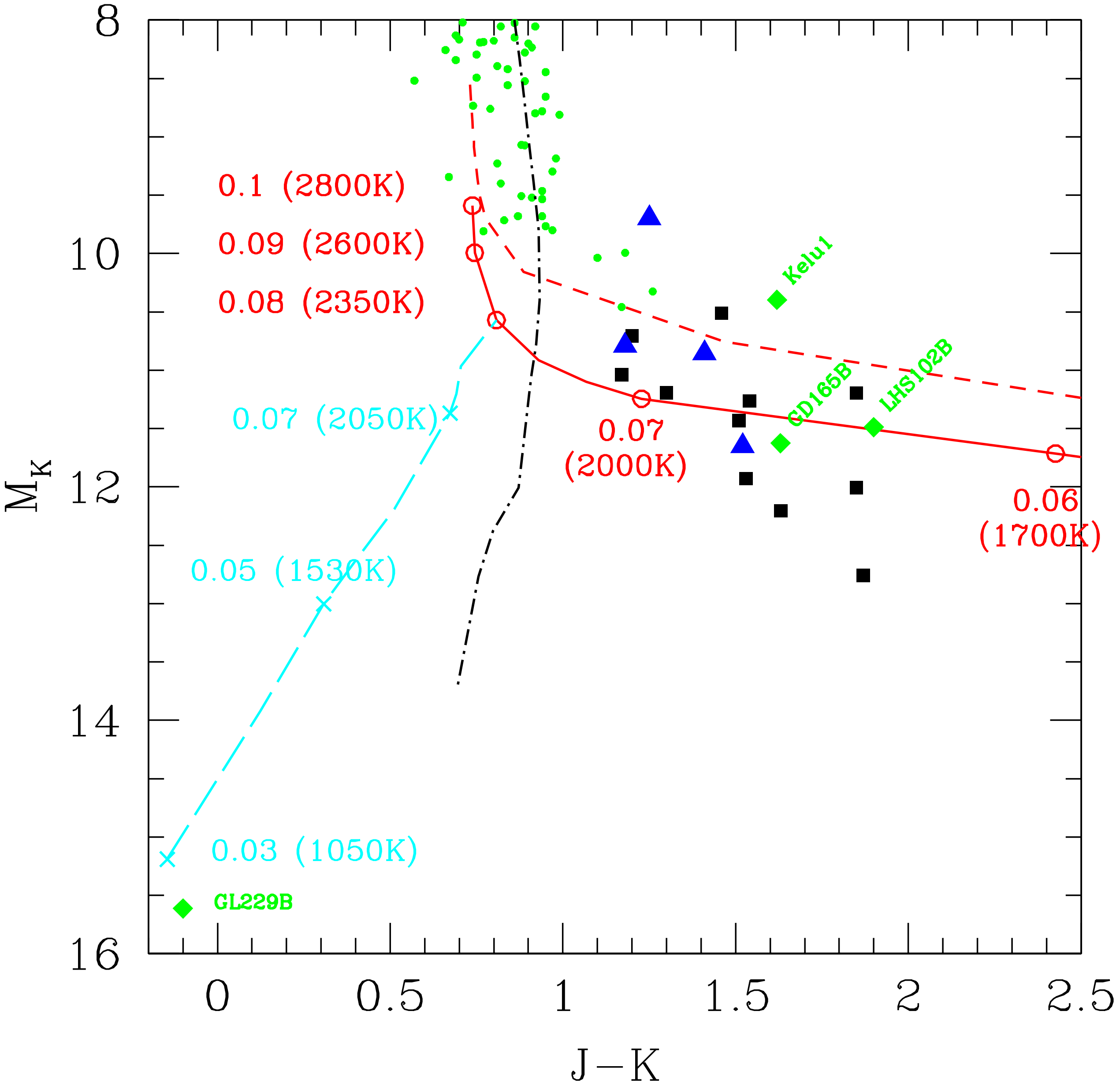

8
10
12
14
16
0
0.5
1
1.5
2
2.5
J−K
M_K
0.1 (2800K)
0.09 (2600K)
0.08 (2350K)
0.07 (2000K)
0.06 (1700K)
0.07 (2050K)
0.05 (1530K)
0.03 (1050K)
Kelu1
GD165B
LHS102B
GL229B

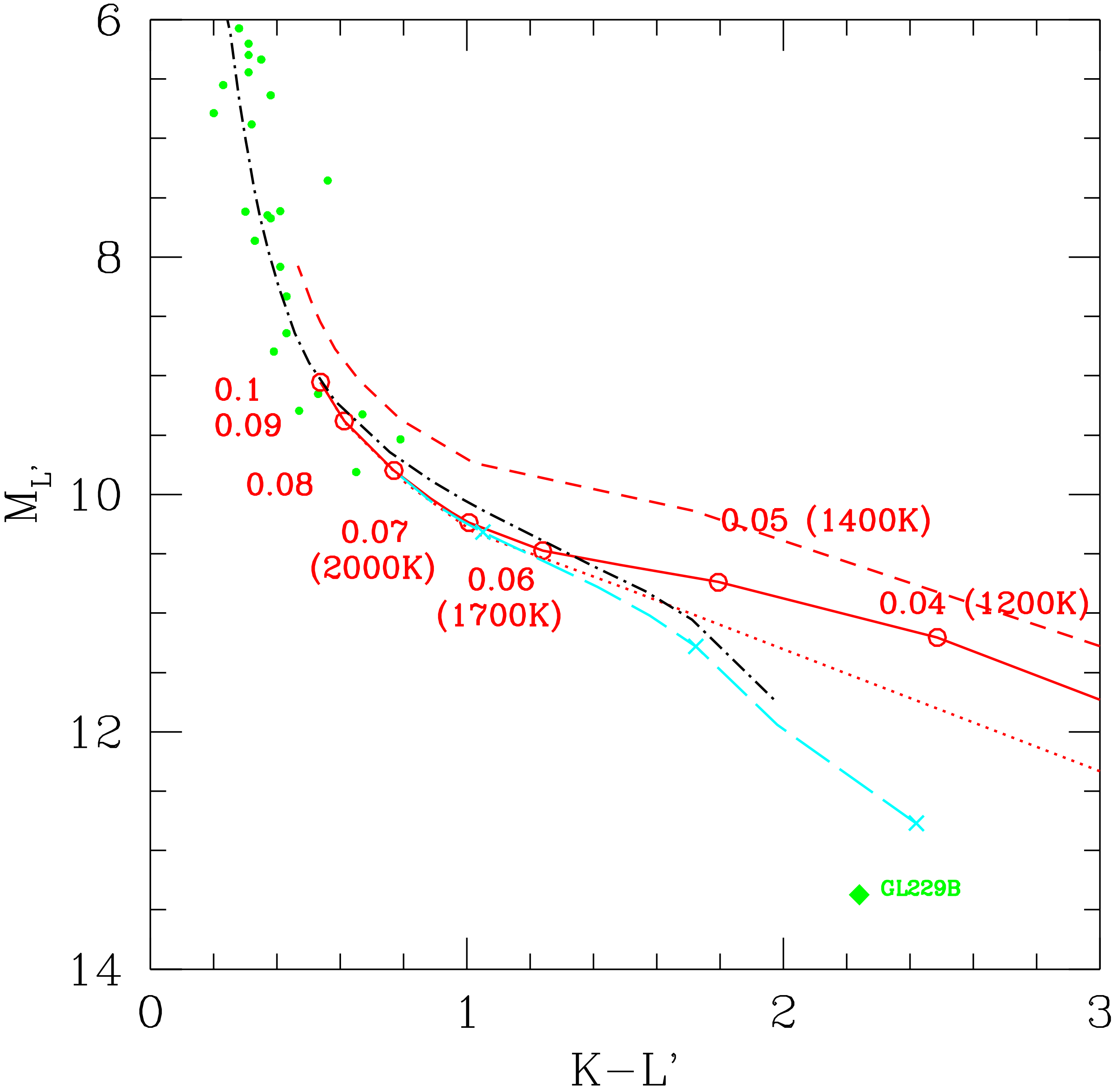

6
8
10
12
14
0
1
2
3
$M_{L'}$
K−L'
0.1
0.09
0.08
0.07
(2000K)
0.06
(1700K)
0.05 (1400K)
0.04 (1200K)
GL229B